Eur. Phys. J. Appl. Phys. **52**, 23309 (2010)
DOI: 10.1051/epjap/2010101

THE EUROPEAN PHYSICAL JOURNAL APPLIED PHYSICS

Regular Article

A perturbation method for the A-χ geometric eddy-current formulation

R. Specogna[1,2,a], P. Dular[1,b], and F. Trevisan[2,c]

[1] Université de Liège, Département d'Électricité, Électronique et Informatique, 4000 Liège, Belgium
[2] Università di Udine, Dipartimento of Ingegneria Elettrica, Gestionale e Meccanica, Via delle Scienze 208, 33100 Udine, Italy

Received: 16 December 2009 / Accepted: 20 May 2010
Published online: 21 October 2010 –

Abstract. A perturbation method for the A-χ geometric formulation to solve eddy-current problems is introduced. The proposed formulation is applied to the feasibility design of a non-destructive evaluation device suitable to detect "long" longitudinal flaws in hot steel bars.

1 Introduction

Industrial companies have a remarkable interest about the techniques for the detection of the surface flaws that can be present during hot mill rolling process of steel bars with circular cross-section (with a diameter from 8 to 80 mm, a speed from 5 to 100 m/s in the longitudinal direction z and a temperature from 800 to 1200 °C).

The capability to detect these flaws permits a fast and straightforward quality assessment of the product and provides the possibility to reduce those flaws due to a wrong set-up of the manufacturing process parameters. The flaws considered have a depth ranging from 0.1 mm to 2 mm and, even though they have quite different shapes and sizes, they generally correspond to an interruption of the material continuity (also from the electrical point of view) and lay almost along an axial direction.

Two main categories of surface flaws can be considered, depending on their axial length L: the "short" flaws, with L ranging from 1 mm to 20 mm and the "long" flaws with L from a meter to tens of meters. In any case, the flaw width is much smaller than the two other dimensions. Short flaws can be easily detected using a differential method in which the signal, after the noise reduction, is compared with a similar signal taken few centimeters away along the axial direction. On the contrary, so far, no practical solution has been found as regards the detection of long flaws, for which a differential approach is not suitable.

In this paper, the feasibility design of a possible configuration able to detect the long flaws is addressed. The numerical simulations have been performed by means of the A-χ geometric formulation [1]. To solve the forward problem efficiently, a perturbation method suitable with the A-χ formulation is proposed. The advantages over the classical A-χ formulation are discussed.

[a] e-mail: ruben.specogna@uniud.it
[b] e-mail: patrick.dular@ulg.ac.be
[c] e-mail: trevisan@uniud.it

2 The A-χ geometric formulation

The so-called "discrete geometric approach" (DGA) [2–4], similarly to the finite integration technique (FIT) [5] or the cell method [6,7], allows to solve directly Maxwell's equations in an alternative way with respect to the classical Galerkin method in finite elements.

The domain of interest D of the eddy-current problem, has been partitioned into a source region D_s and in a passive conductive region D_c. The complement of $D_c \bigcup D_s$ in D represents the air region D_a.

We introduce in D a pair of interlocked cell complexes using *barycentric subdivision* [6] for the dual complex and we denote by $\mathbf{G}$ the incidence matrix between edges e and nodes n, by $\mathbf{C}$ the incidence matrix between faces f and edges e and by $\mathbf{D}$ the incidence matrix between cells v and faces f. The matrices $\tilde{\mathbf{G}} = \mathbf{D}^T$, $\tilde{\mathbf{C}} = \mathbf{C}^T$ and $\tilde{\mathbf{D}} = -\mathbf{G}^T$ describe the mutual interconnections of the dual barycentric complex (dual volumes $\tilde{v}$, dual faces $\tilde{f}$, dual edges $\tilde{e}$, dual nodes $\tilde{n}$).

Next, we consider the integrals of the field quantities with respect to the oriented geometric elements of the mesh, yielding the Degrees of Freedom (DoF) arrays. Each entry of a DoF array is indexed over the corresponding geometric element. There is a univocal association between a global variable and the corresponding geometric element [8]. We introduce the following arrays of DoFs:

– $\boldsymbol{\Phi}$ is the array of magnetic fluxes associated with faces $f \in D$;

– **F** is the array of m.m.f.s associated with dual edges $\tilde{e} \in D$;
– **I** is the array of currents associated with dual faces $\tilde{f} \in D_c$. In D_s we introduce the array $\mathbf{I}_s$ of impressed currents;
– **U** is the array of e.m.f.s associated with primal edges $e \in D_c$.

We introduce also the following arrays of DoFs relative to the potentials used in this formulation:

– **A** is the array of circulations of the magnetic vector potential A along the primal edges $e \in D$;
– $\boldsymbol{\chi}$ is the array of the electric scalar potential χ associated with primal nodes $n \in D_c$.

Within the framework of the DGA, Maxwell's laws can be written *exactly* as topological balance equations between DoFs arrays, as

$$\mathbf{C}^T\mathbf{F} = \mathbf{I}_t \tag{1a}$$
$$\boldsymbol{\Phi} = \mathbf{C}\mathbf{A} \tag{1b}$$
$$\mathbf{G}_c^T\mathbf{I} \tag{1c}$$

where (1a) is the Ampère's balance law, (1b) assures that Gauss' balance law $\mathbf{D}\boldsymbol{\Phi} = 0$ is satisfied identically (since $\mathbf{DC} = 0$) and (1c) is the balance continuity law. $\mathbf{G}_c$ is the sub-matrix of $\mathbf{G}$ relative to the edges and nodes in D_c and $(\mathbf{I}_t)_e$ is equal to $(\mathbf{I})_e$ for edges $e \in D_c$, $(\mathbf{I}_s)_e$ for edges $e \in D_s$ and zero elsewhere.

The discrete counterparts of the constitutive laws can be written as

$$\mathbf{F} = \boldsymbol{\nu}\,\boldsymbol{\Phi} \ \text{ in } D \tag{2a}$$
$$\mathbf{I} = \boldsymbol{\sigma}\,\mathbf{U} \ \text{ in } D_c \tag{2b}$$

where the construction of the matrices $\boldsymbol{\nu}$ and $\boldsymbol{\sigma}$, called constitutive matrices, will be addressed in Section 3.

Combining discrete Faraday's law $(\mathbf{CU})_f = -i\omega(\boldsymbol{\Phi})_f$, with $f \in D_c$, with (1b), we can express the e.m.f. associated with an edge $e \in D_c$ as

$$(\mathbf{U})_e = -i\omega\left((\mathbf{A})_e + (\mathbf{G}_c\boldsymbol{\chi})_e\right), \tag{3}$$

since $\mathbf{CG} = 0$ holds identically.

From (1a)–(1c), (2a)–(2b) and (3), the final algebraic system, having **A** and $\boldsymbol{\chi}$ as unknowns [1,9,10], can be written as

$$\begin{aligned}
&\left(\mathbf{C}^T\boldsymbol{\nu}\mathbf{C}\,\mathbf{A}\right)_e = 0 \ \ \forall e \in D_a,\\
&\left(\mathbf{C}^T\boldsymbol{\nu}\mathbf{C}\,\mathbf{A}\right)_e = (\mathbf{I}_s)_e \ \ \forall e \in D_s,\\
&\left(\mathbf{C}^T\boldsymbol{\nu}\mathbf{C}\,\mathbf{A}\right)_e + i\omega\,(\boldsymbol{\sigma}\,\mathbf{A}_c)_e + i\omega\,(\boldsymbol{\sigma}\mathbf{G}_c\,\boldsymbol{\chi})_e = 0 \ \ \forall e \in D_c,\\
&i\omega\left(\mathbf{G}_c^T\boldsymbol{\sigma}\,\mathbf{A}_c\right)_n + i\omega\left(\mathbf{G}_c^T\boldsymbol{\sigma}\mathbf{G}_c\,\boldsymbol{\chi}\right)_n = 0 \ \ \forall n \in D_c,
\end{aligned} \tag{4}$$

where the array $\mathbf{A}_c$ is the sub-array of **A**, associated with primal edges in D_c. With the notation $(\mathbf{x})_k$, we mean the kth row of array $\mathbf{x}$, where $k = \{e, n\}$ is the label of edge e or of node n.

As boundary conditions we impose $(\mathbf{A})_e = 0$ on $e \in \partial D$ and solve the singular linear system of equations with a CG method without gauge condition.

3 Constitutive matrices

The square matrix $\boldsymbol{\nu}$ ($\dim(\boldsymbol{\nu}) = N_f$, N_f being the number of faces in D) is the reluctance matrix such that (2a) holds exactly at least for an element-wise *uniform* induction field B and magnetic field H in each tetrahedron and it is the approximate discrete counterpart of the constitutive relation $H = \nu\,B$ at continuous level, ν being the reluctivity assumed element-wise a constant.

The square matrix $\boldsymbol{\sigma}$ ($\dim(\boldsymbol{\sigma}) = N_{e_c}$, N_{e_c} being the number of edges in D_c) is the conductance matrix such that (2b) holds exactly at least for an element-wise *uniform* electric field E and current density J in each tetrahedron and it is the approximate discrete counterpart of the constitutive relation $J = \sigma\,E$ at continuous level, σ being the conductance assumed element-wise a constant.

Classical ways to construct the constitutive matrices $\boldsymbol{\nu}$ and $\boldsymbol{\sigma}$ for a tetrahedral mesh are the Discrete Hodge technique based on Whitney's maps, described in [11] or the so called Galerkin Hodge [12], that produce the same stiffness matrix as the Finite Elements with first order edge element basis functions. With the first solution the obtained matrix is non-symmetric, but it's possible to demonstrate that, if the Whitney's functions are evaluated in the center of mass of the tetrahedron, the matrix $\boldsymbol{\sigma}$ becomes symmetric [9].

Another original solution is to use the edge and face vector basis functions defined in [13] for tetrahedra and triangular prisms. As proven in [13], these basis functions assure that symmetry, positive-definiteness, and consistency[1] properties are satisfied for all constitutive matrices.

For our application, an hexahedral mesh will be particularly effective. The construction of the constitutive matrices, called also Discrete Hodge operators, for an hexahedral mesh is addressed for example in [14], where a consistent but non-symmetric matrix is constructed. In this paper we will use the original solution presented in [15], which guarantee symmetry, positive-definiteness, and consistency of the constitutive matrices. In [15] it is also shown that the constitutive matrices obtained by the Galerkin Hodge are not consistent in the case of hexahedral meshes, thus are not suitable within the DGA framework.

The main advantage of the DGA with respect to the correspondent Finite Element formulation is that the construction of the stiffness matrix is faster, since no numerical evaluation of a volume integral is needed, being the constitutive matrices constructed geometrically.

4 Integral sources

We can express the array **A** as $\mathbf{A} = \mathbf{A}_s + \mathbf{A}_r$, where $\mathbf{A}_s$ is the array of circulations of the contribution to the magnetic vector potential produced by the source currents in D_s and $\mathbf{A}_r$ is the array of circulations of the contribution

[1] A precise definition of the notion of consistency for constitutive matrices is given in [4].

to the magnetic vector potential due to the eddy-currents in D_c. Therefore we have that

$$\begin{aligned} \left(\mathbf{C}^T\boldsymbol{\nu}\mathbf{C}\,\mathbf{A}_s\right)_e &= (\mathbf{I}_s)_e \quad \left(\mathbf{C}^T\boldsymbol{\nu}\mathbf{C}\,\mathbf{A}_r\right)_e = 0 \quad \forall e \in D_s \\ \left(\mathbf{C}^T\boldsymbol{\nu}\mathbf{C}\,\mathbf{A}_s\right)_e &= 0 \quad \left(\mathbf{C}^T\boldsymbol{\nu}\mathbf{C}\,\mathbf{A}_r\right)_e = (\mathbf{I})_e \;\forall e \in D_c \end{aligned} \tag{5}$$

holds. Each entry $(\mathbf{A}_s)_{e_i}$ of the array $\mathbf{A}_s$ can be precomputed as $(\mathbf{A}_s)_i = \int_{e_i} \mathrm{A}_s \cdot dl$, where e_i is a primal edge in D and A_s is the magnetic vector potential due to the known source current density in D_s.

Here we will consider stranded circular coils, thus A_s can be computed in closed form in terms of the elliptic integrals of the first and second kind [16].

In this way, we can rewrite the system (4) by removing the source currents from its right hand side, obtaining

$$\begin{aligned} &\left(\mathbf{C}^T\boldsymbol{\nu}\mathbf{C}\,\mathbf{A}_r\right)_e = 0 \;\forall e \in D - D_c, \\ &\left(\mathbf{C}^T\boldsymbol{\nu}\mathbf{C}\,\mathbf{A}_r\right)_e + i\omega\,(\boldsymbol{\sigma}\,\mathbf{A}_{cr})_e + i\omega\,(\boldsymbol{\sigma}\mathbf{G}_c\,\boldsymbol{\chi})_e = \\ &\qquad\qquad (\mathbf{v})_e \;\forall e \in D_c, \\ &i\omega\left(\mathbf{G}_c^T\boldsymbol{\sigma}\,\mathbf{A}_{cr}\right)_n + i\omega\left(\mathbf{G}_c^T\boldsymbol{\sigma}\mathbf{G}_c\,\boldsymbol{\chi}\right)_n = (\mathbf{w})_n \;\forall n \in D_c, \end{aligned} \tag{6}$$

where $\mathbf{v} = -i\omega\boldsymbol{\sigma}\,\mathbf{A}_{cs}$ and $\mathbf{w} = \mathbf{G}_c^T\mathbf{v}$. $\mathbf{A}_{cr}$ and $\mathbf{A}_{cs}$ are the sub-arrays of $\mathbf{A}_r$ and $\mathbf{A}_s$ containing the DoFs associated with primal edges in D_c.

5 Perturbation method for A-χ

We will indicate with the superscript ^{u} and ^{p} the quantities in the unperturbed and perturbed configurations respectively. For the unperturbed configuration we write:

$$\begin{aligned} &\left(\mathbf{C}^T\boldsymbol{\nu}\mathbf{C}\,\mathbf{A}_r^u\right)_e = 0, \\ &\left(\mathbf{C}^T\boldsymbol{\nu}\mathbf{C}\,\mathbf{A}_r^u\right)_e + i\omega\,(\boldsymbol{\sigma}^u\,(\mathbf{A}_{cr}^u + \mathbf{G}_c\boldsymbol{\chi}^u + \mathbf{A}_{cs}))_e = 0, \\ &i\omega\,\left(\mathbf{G}_c^T\boldsymbol{\sigma}^u\,(\mathbf{A}_{cr}^u + \mathbf{G}_c\boldsymbol{\chi}^u + \mathbf{A}_{cs})\right)_n = 0. \end{aligned} \tag{7}$$

In the perturbed case the distribution of σ^p differs from the distribution in the unperturbed case σ^u

$$\begin{aligned} &\left(\mathbf{C}^T\boldsymbol{\nu}\mathbf{C}\,\mathbf{A}_r^p\right)_e = 0, \\ &\left(\mathbf{C}^T\boldsymbol{\nu}\mathbf{C}\,\mathbf{A}_r^p\right)_e + i\omega\,(\boldsymbol{\sigma}^p\,(\mathbf{A}_{cr}^p + \mathbf{G}_c\boldsymbol{\chi}^p + \mathbf{A}_{cs}))_e = 0, \\ &i\omega\,\left(\mathbf{G}_c^T\boldsymbol{\sigma}^p\,(\mathbf{A}_{cr}^p + \mathbf{G}_c\boldsymbol{\chi}^p + \mathbf{A}_{cs})\right)_n = 0. \end{aligned} \tag{8}$$

Next, we consider the difference between the perturbed (^{p}) configuration and the unperturbed (^{u}) configuration, while keeping constant the source currents. We will indicate with $\mathbf{A}^v = \mathbf{A}^p - \mathbf{A}^u = \mathbf{A}_r^p - \mathbf{A}_r^u$ and $\boldsymbol{\chi}^v = \boldsymbol{\chi}^p - \boldsymbol{\chi}^u$ the corresponding differences. The difference will be

$$\begin{aligned} &\left(\mathbf{C}^T\boldsymbol{\nu}\mathbf{C}\,\mathbf{A}^v\right)_e = \mathbf{0}, \\ &\left(\mathbf{C}^T\boldsymbol{\nu}\mathbf{C}\,\mathbf{A}^v\right)_e + i\omega\,(\boldsymbol{\sigma}^p\,(\mathbf{A}_{cr}^p + \mathbf{G}_c\boldsymbol{\chi}^p + \mathbf{A}_{cs}) \\ &\qquad -i\omega\,\boldsymbol{\sigma}^u\,(\mathbf{A}_{cr}^u + \mathbf{G}_c\boldsymbol{\chi}^u + \mathbf{A}_{cs}))_e = 0, \\ &i\omega\,\left(\mathbf{G}_c^T\boldsymbol{\sigma}^p\,(\mathbf{A}_{cr}^p + \mathbf{G}_c\boldsymbol{\chi}^p + \mathbf{A}_{cs})\right. \\ &\qquad \left. -i\omega\,\mathbf{G}_c^T\boldsymbol{\sigma}^u\,(\mathbf{A}_{cr}^u + \mathbf{G}_c\boldsymbol{\chi}^u + \mathbf{A}_{cs})\right)_n = 0. \end{aligned} \tag{9}$$

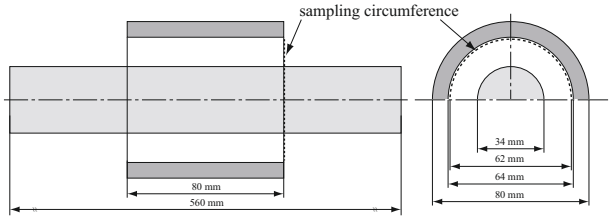

Fig. 1. The geometry of the eddy-currents problem.

Now we add and subtract to the second equation the following quantity $i\omega\,\boldsymbol{\sigma}^p\,(\mathbf{A}_{cr}^u + \mathbf{G}_c\boldsymbol{\chi}^u + \mathbf{A}_{cs})$; similarly to the third equation we add and subtract the following quantity $i\omega\,\mathbf{G}_c^T\boldsymbol{\sigma}^p\,(\mathbf{A}_{cr}^u + \mathbf{G}_c\boldsymbol{\chi}^u + \mathbf{A}_{cs})$. Then (9) becomes

$$\begin{aligned} &\left(\mathbf{C}^T\boldsymbol{\nu}\mathbf{C}\,\mathbf{A}^v\right)_e = \mathbf{0}, \\ &\left(\mathbf{C}^T\boldsymbol{\nu}\mathbf{C}\,\mathbf{A}^v\right)_e + i\omega\,(\boldsymbol{\sigma}^p\,(\mathbf{A}^v + \mathbf{G}_c\boldsymbol{\chi}^v) + i\omega\,(\boldsymbol{\sigma}^p - \boldsymbol{\sigma}^u) \\ &\qquad \times (\mathbf{A}_{cr}^u + \mathbf{G}_c\boldsymbol{\chi}^u + \mathbf{A}_{cs}))_e = 0, \\ &i\omega\,\left(\mathbf{G}_c^T\boldsymbol{\sigma}^p\,(\mathbf{A}^v + \mathbf{G}_c\boldsymbol{\chi}^v) + i\omega\,\mathbf{G}_c^T\,(\boldsymbol{\sigma}^p - \boldsymbol{\sigma}^u)\right. \\ &\qquad \left. \times (\mathbf{A}_{cr}^u + \mathbf{G}_c\boldsymbol{\chi}^u + \mathbf{A}_{cs})\right)_n = 0, \end{aligned} \tag{10}$$

where the term

$$i\omega\,(\boldsymbol{\sigma}^p - \boldsymbol{\sigma}^u)\,(\mathbf{A}_{cr}^u + \mathbf{G}_c\boldsymbol{\chi}^u + \mathbf{A}_{cs}) = \mathbf{I}_d \tag{11}$$

represents a known impressed current $\mathbf{I}_d$ in the flaw region only; $\mathbf{I}_d$ depends on the quantities computed in the unperturbed (^{u}) configuration and on the sources $\mathbf{A}_s$. We rewrite (10) as

$$\begin{aligned} &\left(\mathbf{C}^T\boldsymbol{\nu}\mathbf{C}\,\mathbf{A}^v\right)_e = \mathbf{0} \;\forall e \in D - D_c, \\ &\left(\mathbf{C}^T\boldsymbol{\nu}\mathbf{C}\,\mathbf{A}^v\right)_e + i\omega\,(\boldsymbol{\sigma}^p\,(\mathbf{A}^v + \mathbf{G}_c\boldsymbol{\chi}^v))_e = -\,(\mathbf{I}_d)_e \;\forall e \in D_c, \\ &i\omega\,\left(\mathbf{G}_c^T\boldsymbol{\sigma}^p\,(\mathbf{A}^v + \mathbf{G}_c\boldsymbol{\chi}^v)\right)_n = -\left(\mathbf{G}_c^T\mathbf{I}_d\right)_n \;\forall n \in D_c. \end{aligned} \tag{12}$$

From (12), we obtain directly the solution due to the perturbation, reducing the cancelation error [17,18].

6 Application to non-destructive testing

The application concerns the design of a device for the detection of long longitudinal flaws that can be present during the hot mill rolling process of the steel bars with circular cross-section.

The geometry of the problem, depicted in Figure 1, consists of a conducting AISI 310 steel bar, modeled as a conducting cylinder D_c. The radius of the bar is 17 mm and the conductivity is $\sigma = 1.236 \times 10^6$ S/m. A longitudinal perfectly insulating surface flaw is assumed, 0.5 mm deep from the surface of the cylinder and 0.2 mm thick.

A source coil D_s (32 mm inner radius, 40 mm outer radius, 80 mm height, 640 turns) encircles the rod and is feeded by a sinusoidal current density of 10^6 A/m^2 with a frequency of $f = 100$ kHz. Since the rod is hot, the lift-off is chosen to be 15 mm.

Unlike usual NDT methods that use global quantities, usually the impedance variation of the receiving coils, the

sensors sample B on points distributed over a circumference. We choose the circumference to lie in the plane $z = 40$ mm, with a radius of 31 mm and the center on the axis of the coil, see Figure 1. The sampling circumference is considered fixed with the coil, since in practice the coil and the receiving sensors are assembled together.

Unlike usual NDT methods that use global quantities, usually the impedance variation of the receiving coils, the sensors sample B on points distributed over a circumference. We choose the circumference to lie in the plane $z = 40$ mm, with a radius of 31 mm and the center on the axis of the coil, see Figure 1. The sampling circumference is considered fixed with the coil, since in practice the coil and the receiving sensors are assembled together.

The variation of the tangential component of B along the sampling points due to the presence of a flaw will be analyzed and compared with the one obtained from the difference between the perturbed and unperturbed solutions.

6.1 Magnetic induction field computation

To calculate the value of the induction magnetic field B components in a sample point P, two different approaches can be used:

(i) Find the hexahedron whose P belong. Calculate $\mathbf{A} = \mathbf{A}_r + \mathbf{A}_s$ over the twelve edges. Find the magnetic fluxes through the four faces with $\boldsymbol{\Phi} = \mathbf{CA}$ and finally interpolate $B(\mathrm{P})$ using the magnetic fluxes inside the hexahedron with the face basis functions.

(ii) Using the Biot-Savart Law:

$$B(\mathrm{P}) = B_s(\mathrm{P}) + \frac{\mu_0}{4\pi} \int_{D_c} \frac{J(\mathrm{P}') \times \hat{r}}{r^2} dV,$$

where B_s is the magnetic induction produced by the source coil and $\hat{r}$ is the unit vector directed as the segment PP′.

The second solution is preferable, in fact, being B the result of a global evaluation, it yields a more accurate value. The volume integral is computed using three Gauss's points.

7 Numerical results

An extruded mesh with about $313\,k$ hexahedra, yielding more then 1.1 million of DoFs, is used for the computations, see Figure 2. Thanks to integral representation of sources, this mesh will not be changed in all the simulations, even when the source coil is moved. Since in general it is a full three-dimensional problem, we cannot take advantage of any symmetry.

7.1 Validation

The code is validated comparing the results in terms of current density and magnetic induction with respect to a two-dimensional axisymmetrical FEM simulation. In Figure 3 the current density along a sampling line ($x = 2 \times 10^{-5}$ m; $y = 16.95$ mm; $z = -150/150$ mm) shows very good agreement. In Figures 4 and 5 the magnetic induction is compared along a sampling line ($x = 2 \times 10^{-5}$ m; $y = 31$ mm; $z = 0/100$ mm) with the FEM simulation. As we were expecting, the postprocessing using the Biot-Savart law is more accurate and will be used for further evaluations of the magnetic induction.

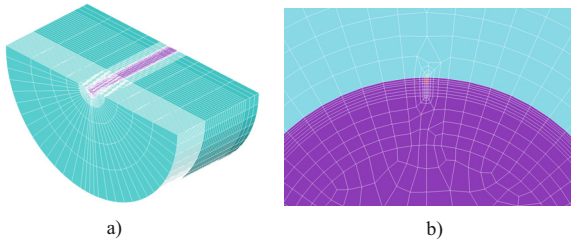

a) b)

Fig. 2. (Color online) (a) One fourth of the hexahedral mesh used in the NDT application. (b) A zoom on the mesh in the neighborhood of the flaw.

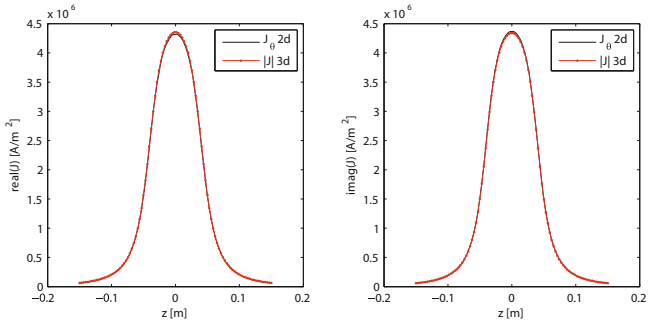

Fig. 3. (Color online) The computed current density J (real part on the left, imaginary part on the right) along a sampling line in the case of unperturbed problem, compared with an axisymmetrical two-dimensional FEM simulation.

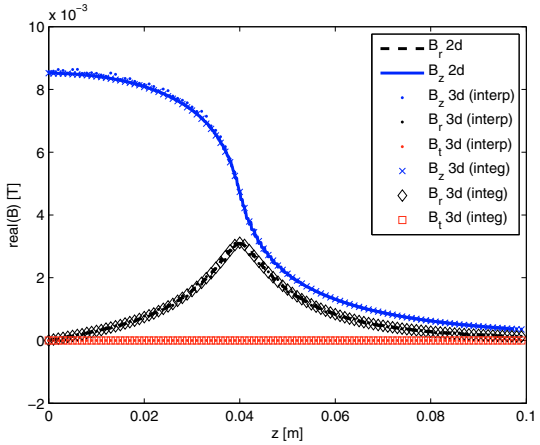

Fig. 4. (Color online) The computed real part of the induction magnetic field B along a sampling line in the case of unperturbed problem, compared with an axisymmetrical two-dimensional FEM simulation. B is found both with direct interpolation (interp) and using the Biot-Savart law (integ).

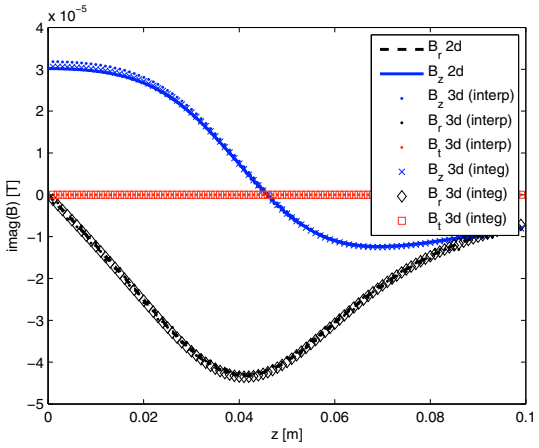

Fig. 5. (Color online) The computed imaginary part of the induction magnetic field B along a sampling line in the case of unperturbed problem, compared with an axisymmetrical two-dimensional FEM simulation. B is found both with direct interpolation (interp) and using the Biot-Savart law (integ).

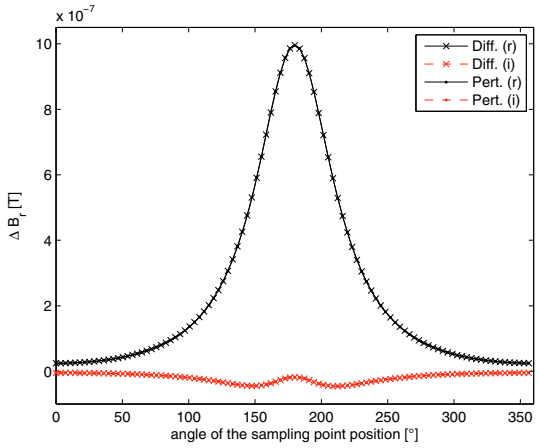

Fig. 7. (Color online) Variation due to the flaw on the radial component. (pert.) denote the value obtained with perturbation, while (diff.) the value obtained with difference between the perturbed and unperturbed solutions. (r) denotes the real part, (i) the imaginary part.

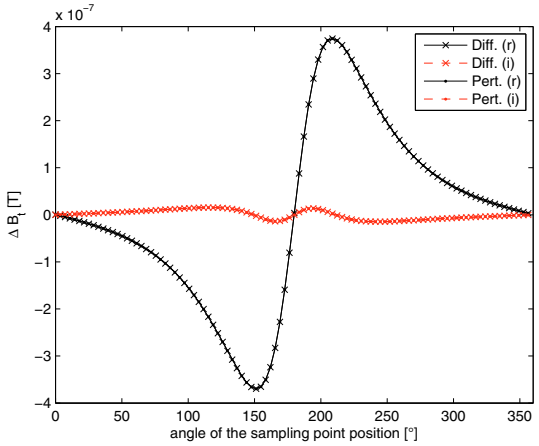

Fig. 6. (Color online) Variation due to the flaw on the tangential component. (pert.) denote the value obtained with perturbation, while (diff.) the value obtained with difference between the perturbed and unperturbed solutions. (r) denotes the real part, (i) the imaginary part.

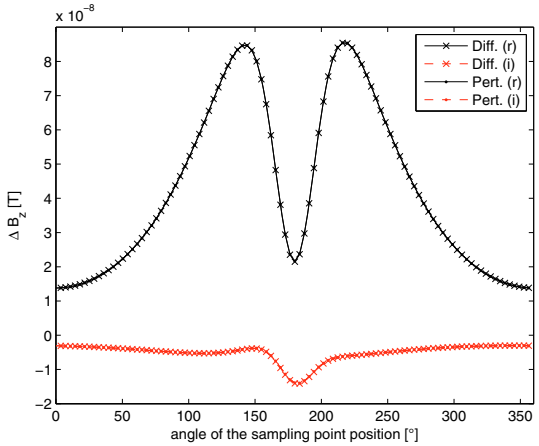

Fig. 8. (Color online) Variation due to the flaw on the longitudinal (z) component. (pert.) denote the value obtained with perturbation, while (diff.) the value obtained with difference between the perturbed and unperturbed solutions. (r) denotes the real part, (i) the imaginary part.

7.2 Magnetic induction variation due to the flaw

After the code validation, we compute the variation of the magnetic induction on the sampling circumference due to the flaw. At first, this is achieved by computing the difference between the perturbed and unperturbed solutions. Then, the magnetic induction variation is directly computed by means of the perturbation method. In Figures 6, 7 and 8 the magnetic induction variations of the tangential, radial and z components are shown respectively. The flaw is placed at 180° and produces a perturbation on the tangential B field that changes sign passing from one side of the flaw to the other. The two alternative methods to compute such a variation are in very good agreement.

The perturbation method allows to produce more accurate results at a less computational effort. The accuracy improvement is due to the reduction of the cancelation error. This becomes fundamental especially when the formulation is used as a forward solver for an inverse problem. In this case, in fact, the variation at every iteration becomes smaller and smaller, requiring a good immunity to the cancelation error.

The perturbation method also reduces the computational time. The resulting linear system of equations, in fact, converges more rapidly and no post-processing is needed for the unperturbed simulation. Moreover, the computation time of the source current $\mathbf{I}_d$ is negligible and smaller then the calculation of the source $\mathbf{v}$.

A further reduction of the computational time is obtained by observing that the source of the perturbation problem is localized into the flaw region. Consequently, the perturbation in the current density will be concentrated in

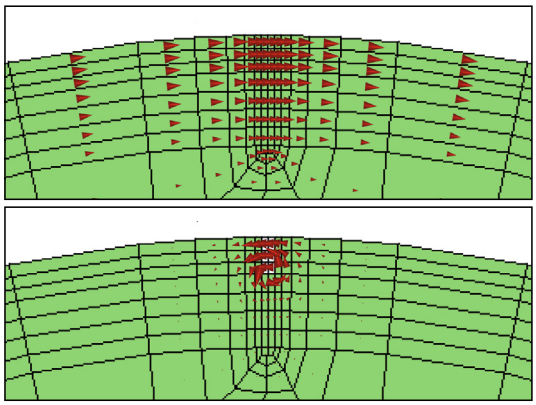

Fig. 9. (Color online) On the top, the current density in the neighborhood of the flaw obtained using the unperturbed configuration. On the bottom, the current density obtained with the perturbation problem, which is confined in the neighborhood of the flaw.

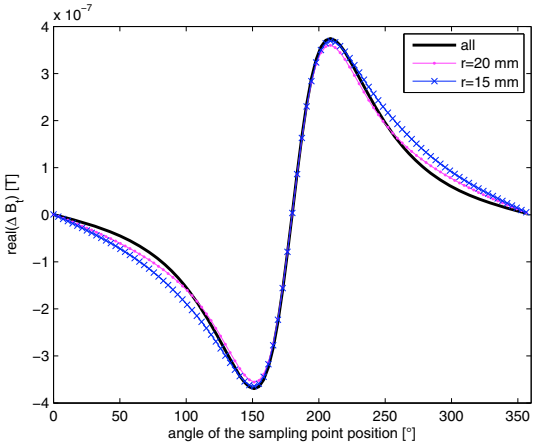

Fig. 10. (Color online) The real part of the tangential component of the magnetic induction due to the flaw obtained with the reduced meshes is compared to the one obtained with the original mesh.

a neighborhood of the flaw, see for example Figure 9. For this reason, the initial mesh can be dramatically reduced considering only the hexahedra contained in a limited region surrounding the flaw.

In this paper, the reduced mesh is constructed keeping only the hexahedra with the center of mass contained into the cylinder $(x - 16.5\ \text{mm})^2 + y^2 = r^2$. Two cases are considered, with radiuses of 20 mm and 15 mm. The hexahedra are reduced from $313\,k$ of the original mesh to respectively $114\,k$ and $80\,k$. In Figure 10 the variation in the real part of the tangential component of the magnetic induction due to the flaw obtained with the reduced meshes are compared with the original one.

The accuracy can be further improved if a different and more refined mesh is created around the flaw. In this case, the impressed current $\mathbf{I}_d$ has to be projected onto the new mesh [18].

8 Conclusions

The perturbation method, reducing the cancelation error, produces accurate results also for small variations in the solution. This is especially required when the tool is used as a forward solver for an inverse problem. Moreover the method yields also a considerable speed-up: the mesh used in the perturbed problem can in fact be reduced, considering only a limited region surrounding the flaw, at a small fraction of the initial mesh.

References

1. F. Trevisan, IEEE Trans. Magn. **40**, 1314 (2004)
2. F.H. Branin Jr., The Algebraic-Topological Basis for Network Analogies and the Vector Calculus, in *Proc. Symp. on Generalized Networks* (Polytechnic Press, Brooklin, NY, 1966), pp. 453–491
3. A. Bossavit, IEEE Trans. Magn. **34**, 2429 (1998)
4. A. Bossavit, L. Kettunen, IEEE Trans. Magn. **36**, 861 (2000)
5. M. Clemens, T. Weiland, PIER Monograph Ser. **32**, 65 (2001)
6. E. Tonti, Algebraic topology and computational electromagnetism, in *4th Int. Workshop on Electric and Magnetic Fields, Marseille, France, 1988*, pp. 284–294
7. E. Tonti, in *Gravitation, Electromagnetism and Geometrical Structures* (Pitagora Editrice, Bologna, 1995), pp. 281–308
8. E. Tonti, *On the formal structure of physical theories* (Monograph of the Italian National Research Council, 1975)
9. R. Specogna, F. Trevisan, IEEE Trans. Magn. **41**, 1259 (2005)
10. F. Trevisan, L. Kettunen, Int. J. Num. Meth. Eng. **67**, 1888 (2006)
11. T. Tarhasaari, L. Kettunen, A. Bossavit, IEEE Trans. Mag. **35**, 1494 (1999)
12. A. Bossavit, J. Jpn Soc. Appl. Electromagn. Mech. **8**, 203 (2000)
13. L. Codecasa, R. Specogna, F. Trevisan, IEEE Trans. Magn. **42**, 510 (2007)
14. P. Dular, R. Specogna, F. Trevisan, IEEE Trans. Mag. **44**, 694 (2008)
15. L. Codecasa, R. Specogna, F. Trevisan, CMES Comput. Modeling Eng. Sci. **31**, 129 (2008)
16. E. Durand, *Magnétostatique* (Masson et Cie, Paris, 1968)
17. R. Albanese, G. Rubinacci, F. Villone, J. Comput. Phys. **152**, 736 (1999)
18. R.V. Sabariego, P. Dular, IEEE Trans. Magn. **43**, 1289 (2007)